APPLIED PHYSICS

Revealing the key role of molecular packing on interface spin polarization at two-dimensional limit in spintronic devices

Zhongzhong Luo[1,2]*†, Xiangxiang Song[2,3]†, Xiaolong Liu[4], Xiangqian Lu[5], Yu Yao[6], Junpeng Zeng[2], Yating Li[2], Daowei He[2], Huijuan Zhao[6], Li Gao[6], Zhihao Yu[2,7], Wei Niu[8], Huabin Sun[7], Yong Xu[7,9], Shujuan Liu[6], Wei Qin[5]*, Qiang Zhao[1,6]*

Understanding spinterfaces between magnetic metals and organic semiconductors is essential to unlock the great potentials that organic materials host for spintronic applications. Although plenty of efforts have been devoted to studying organic spintronic devices, exploring the role of metal/molecule spinterfaces at two-dimensional limit remains challenging because of excessive disorders and traps at the interfaces. Here, we demonstrate atomically smooth metal/molecule interfaces through nondestructively transferring magnetic electrodes on epitaxial grown single-crystalline layered organic films. Using such high-quality interfaces, we investigate spin injection of spin-valve devices based on organic films of different layers, in which molecules are packed in different manners. We find that the measured magnetoresistance and the estimated spin polarization increase markedly for bilayer devices compared with their monolayer counterparts. These observations reveal the key role of molecular packing on spin polarization, which is supported by density functional theory calculations. Our findings provide promising routes toward designing spinterfaces for organic spintronic devices.

INTRODUCTION

Because of the advantages of weak spin-orbit coupling and hyperfine interaction, organic materials are promising for spintronic applications (*1*–*6*). A variety of devices have been demonstrated including spin valves, spin memory devices, and light-emitting diodes (*7*–*9*). It is expected that the spinterfaces between organic semiconductors and ferromagnetic (FM) metals, which are sensitive to structural properties and side chain substitution of the molecules, play an important role in these spintronic devices (*10*–*14*). However, there are still several obstacles lying ahead for fully understanding these molecular spinterfaces from the experimental point of view, thus limiting the device applications based on organic materials. First, organic semiconductors with high mobility and low density of disorders/traps are rarely implemented, preventing further fabrication of high-quality interfaces. Second, evaporation of FM metals on organic semiconductors usually damages the adjacent molecular layers (*15*), leading to degraded quality of the interface. These challenges make researchers investigate spinterfaces by absorbing organic molecules on FM metals alternatively (*11*, *16*), instead of studying them from the device perspective.

Here, we report organic spin valves (OSVs) with minimal disorders both in organic crystals and at the interfaces. The devices are based on two-dimensional (2D) layered molecular crystals, which have attracted considerable interests owing to their high carrier mobility, tunable light-matter interaction, and high sensitivity to external stimuli (*17*–*21*). These materials could be synthesized through van der Waals (vdW) epitaxial growth on substrates of 2D inorganic materials, allowing the formation of atomically smooth single-crystalline organic films down to monolayers (*22*, *23*). Furthermore, to avoid potential damages to organic crystals during electrode integration, we use the vdW metal-transfer technique, which has been developed for electronic applications based on organic (*24*) and 2D inorganic materials (*25*–*27*). Using this technique, FM electrodes can be gently deposited (*4*) on organic layers for spin injection and detection. With such high-quality interfaces, we are able to investigate interface spin polarization of OSVs based on 2D organic crystals (2,7-dioctyl[1]benzothieno[3,2-b][1]benzothiophene, C_8-BTBT, in this work) of different layers, in which molecular packing plays an important role. Compared with monolayer (1L) devices, bilayer (2L) devices exhibit higher magnetoresistance (MR) (12.3%) with larger estimated spin polarization (43.4%), reaching the best level obtained from similar devices. We perform density functional theory (DFT) calculations to understand the different behaviors of the spin polarization at the interfaces. The calculated polarized spin density distribution and spin-dependent density of states (DOS) near the Fermi energy are found to be strongly modulated by molecular orientation and packing motif. The vertically standing molecules at the top in 2L crystals transport

[1]College of Electronic and Optical Engineering and College of Flexible Electronics (Future Technology), State Key Laboratory of Organic Electronics and Information Displays, Nanjing University of Posts and Telecommunications, Nanjing 210023, China. [2]National Laboratory of Solid State Microstructures, School of Electronic Science and Engineering, Collaborative Innovation Center of Advanced Microstructures, Nanjing University, Nanjing 210093, China. [3]Suzhou Institute for Advanced Research, University of Science and Technology of China, Suzhou 215123, China. [4]School of New Energy, North China Electric Power University, Beijing 102206, China. [5]School of Physics, State Key Laboratory of Crystal Materials, Shandong University, Jinan 250100, China. [6]Institute of Advanced Materials, Nanjing University of Posts and Telecommunications, Nanjing 210023, China. [7]College of Integrated Circuit Science and Engineering, Nanjing University of Posts and Telecommunications, Nanjing 210023, China. [8]New Energy Technology Engineering Laboratory of Jiangsu Province and School of Science, Nanjing University of Posts and Telecommunications, Nanjing 210023, China. [9]Guangdong Greater Bay Area Institute of Integrated Circuit and System, Guangzhou 510535, China.
*Corresponding author. Email: iamqzhao@njupt.edu.cn (Q.Z.); wqin@sdu.edu.cn (W.Q.); luozz1012@njupt.edu.cn (Z.L.)
†These authors contributed equally to this work.

spins to bottom organic layers more effectively, leading to stronger spin injection for 2L devices. Our results reveal the key role of molecular packing on interface spin polarization for organic spintronic devices and demonstrate the promising future for realizing high-quality spinterfaces using 2D molecular semiconductors and vdW magnetic-electrode integration techniques.

RESULTS

Schematics and devices

Ultrathin C_8-BTBT crystals are epitaxially grown on 2D inorganic materials [exfoliated few-layer graphene (FLG) in this work] in a layer-by-layer fashion, exhibiting well-resolved molecular packing structures. Previous studies have revealed that the molecules of first few layers pack in different ways to form crystals (*22*, *28*). The first grown layer lies on the substrate of FLG, known as the interfacial layer (IL). The next layer stacks with a tilted angle of about 60°, which is referred to as 1L. For simplification, we term crystals consisting of IL and 1L as 1L C_8-BTBT samples in the following text. When additional layers are synthesized, they stack in a different manner. For example, the next layer stands along the vertical direction, referred to as 2L. Similarly, we term such crystals consisting of IL, 1L, and 2L as 2L C_8-BTBT samples. Figure 1 (A and B) shows schematic packing structures of 1L and 2L C_8-BTBT samples, respectively. When magnetic metals are attached to the molecular crystals from the top, the difference in packing structures is expected to result in distinct spin polarizations at the interfaces [see the right panels of Fig. 1 (A and B) for schematics of spin-dependent DOSs near the Fermi level E_F]. This relationship between interface spin polarization and molecular packing can be revealed by investigating magneto-transport behaviors of OSVs based on molecular crystals with high-quality FM metal/molecule interfaces.

Figure 1E shows schematics of the OSV device studied in this work. C_8-BTBT crystal is synthesized on FLG through vdW epitaxy. Two FM electrodes (labeled as FM1 and FM2), made of different magnetic metals to exhibit different coercive fields (see fig. S1), are used to inject and detect the spin current. Note that FM1 is attached to the C_8-BTBT crystal, while FM2 is contacted to FLG. Thus, the exfoliated FLG not only provides atomically flat substrate to epitaxially grow high-quality C_8-BTBT crystal but also acts as a spin transport channel that bridges between FM metals and C_8-BTBT due to its long spin diffusion length (*29*, *30*). Figure 1C shows atomic force microscopy (AFM) images of typical 1L and 2L C_8-BTBT crystals, showing flat and uniform surfaces. The total thickness of the heterojunction, including FLG and 1L (2L) C_8-BTBT crystal, is 3.7 nm (6.7 nm). Furthermore, a high-resolution AFM image of 2L C_8-BTBT film (Fig. 1D) demonstrates its high crystallinity with herringbone-type packing (*22*) and atomically smooth surface.

Given the high-quality few-layer molecular crystals, we fabricate OSV devices by integrating FM electrodes. It is well known that conventional nanofabrication processes including lithography and direct metal evaporation damage adjacent organic films, especially for monolayer samples, severely degrading the quality of the metal/organic interface (*31*). To solve this problem, we use a solvent-free vdW magnetic-electrode integration technology to avoid high-energy exposure and evaporation, eliminating defects and traps at the interfaces. Both FM1 and FM2 electrodes consist of three layers of Au, FM metal ($Fe_{20}Ni_{80}$ for FM1 and Co for FM2), and chemical vapor deposition (CVD) grown monolayer graphene (MLG), as illustrated in the inset of Fig. 1E. The FM electrodes are integrated as follows. We first prepare patterned multilayer FM electrodes on a silicon wafer. Then, the electrodes are mechanically released using a probe and gently transferred onto FLG and organic crystals. Detailed fabrication process can be found in Materials and Methods and fig. S2. Here, the MLG layer has three key functions: (i) FM metals are difficult to be mechanically released from the sacrificial substrate directly because of the strong interfacial adhesion. However, the adhesion between MLG and substrate is relatively weak, ensuring the mechanical release of FM metals (*26*). (ii) MLG protects FM metals from oxidation during the electrode-transfer process. (iii) MLG helps in forming high-performance electrical contacts between FM metals and organic layers (*28*).

The pristine quality of the FM electrode/molecule interface is revealed by high-resolution transmission electron microscopy (TEM). Figure 1F shows a cross-sectional TEM image of a typical 1L device, cutting underneath the electrode of FM1. The 1L C_8-BTBT maintains high quality without any destruction. The interface between C_8-BTBT and FM electrode ($Fe_{20}Ni_{80}$ for FM1) is atomically smooth. Low-magnification TEM image confirms excellent uniformity over several micrometers, covering almost the entire contact area (see fig. S3). To further verify the quality of the interface, energy-dispersive x-ray spectroscopy (EDS) is used to map the elemental distributions near the interface (see Fig. 1G). By mapping the distributions of Ni, Fe, and C, a sharp and nondestructed interface is clearly resolved. No obvious diffusion of Ni or Fe atoms is found in the molecular layer. With such high quality of the damage-free interface, we can study the relationship between interface spin polarization and molecular packing. Note that MLG layer is partially damaged during evaporating FM layer and its interface cannot be well resolved in Fig. 1G. This suggests that vdW magnetic-electrode integration technology is essential for preserving high quality of molecular crystals. To verify this, we fabricate controlled devices using the traditional metal evaporation technique (see fig. S4), in which molecular crystals are damaged during the fabrication process.

Electrical performance and magnetoresistance measurements

To have a better understanding of the transport mechanism, resistances of devices have been studied in the absence of magnetic field first. In addition to 1L and 2L devices, we also fabricate devices based on 3L (trilayer) C_8-BTBT crystals (see fig. S5) and devices without molecular crystals (W/O devices) as controlled devices. Figure 2A shows the statistic results of room temperature resistance obtained from more than 100 devices with different layers of organic crystals. It is clear that the averaged device resistance increases more than one order of magnitude when adding one organic layer (see Fig. 2B), which suggests that tunneling through the organic molecular layers occurs in the transport behavior (*32*). Moreover, the dependence of conductance on temperature has been investigated (see Fig. 2C). For 1L device, the resistance is almost independent of temperature (red circles), suggesting that the tunneling behavior is dominant. However, for 2L device, the resistance increases with decreasing temperature (blue circles), indicating a hopping-like transport behavior. The current-voltage (I-V) characteristics of typical 1L and 2L devices at 10 K are shown in Fig. 2D, from which obvious nonlinearity is observed for the 2L

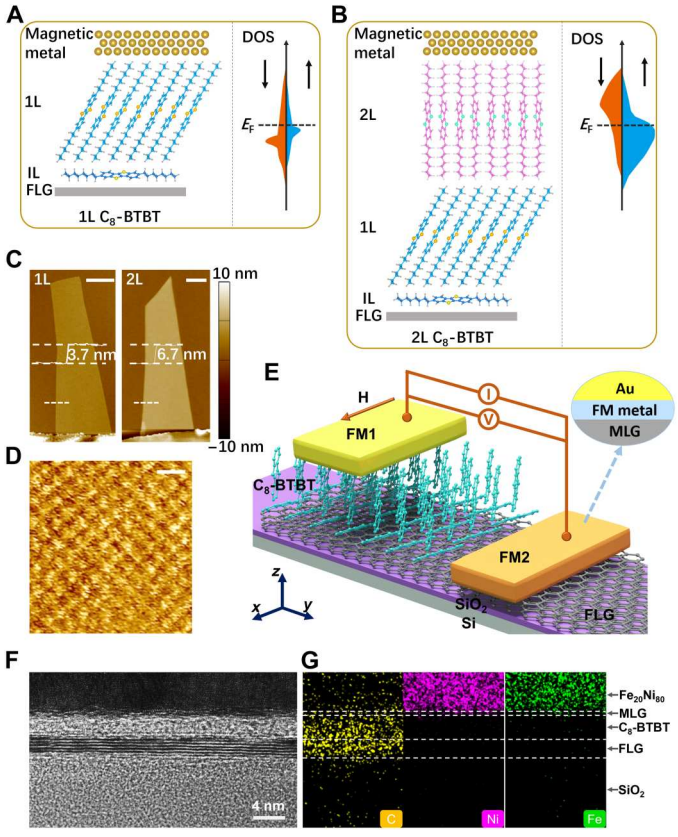

Fig. 1. Schematic illustration and characterization of the device. (**A** and **B**) Schematics of magnetic metals and C_8-BTBT crystals stacked on the substrates of FLG. Organic molecules pack in different manners to form (A) 1L and (B) 2L C_8-BTBT crystals, respectively. The corresponding spin-dependent DOS schematics are shown in the right panels of (A) and (B), respectively. (**C**) Atomic force microscopy (AFM) images of typical 1L (left) and 2L (right) C_8-BTBT crystals before transferring FM1 electrodes, respectively. Scale bars, 1 μm. (**D**) High-resolution AFM image of 2L C_8-BTBT film. Scale bar, 1 nm. (**E**) Schematics of the spin-valve device. C_8-BTBT crystal is synthesized on FLG. Multilayer electrode FM1 (Au/$Fe_{20}Ni_{80}$/MLG) is connected to the C_8-BTBT crystal, while electrode FM2 (Au/Co/MLG) is connected to FLG. The inset illustrates the cross-sectional schematics of multilayer FM electrodes. (**F**) Cross-sectional TEM image and (**G**) corresponding elemental mappings for a typical 1L C_8-BTBT device, cutting underneath the electrode of FM1, respectively. Scale bar, 4 nm.

device. The corresponding differential conductance (dI/dV) curve of the 2L device is plotted in Fig. 2E. It is worth noting that the shape of the dI/dV curve is symmetric and does not show any zero-bias anomaly. Such a behavior indicates that the interface and the barrier are free of magnetic impurities (*33*), which is consistent with the EDS mapping shown in Fig. 1G.

In the following, we conduct MR measurements of devices. Fixing a bias voltage, the current is detected while varying an external in-plane magnetic field. Figure 3 (A and B) shows typical MR curves obtained from 1L (Dev. M1) and 2L devices (Dev. D1), respectively. As the magnetic field is swept from 200 to −200 Oe (blue curve), the magnetizations of the FM electrodes switch from parallel to antiparallel configuration and lastly back to parallel configuration (arrows in Fig. 3, A and B), eliciting the observation of a resistance drop, while for a reversed sweeping direction (red curve), the resistance drop appears at a positive value of magnetic field. The relative MR ratio is defined as $MR = (R_H - R_p)/R_p$, where R_H is the magnetic field–dependent resistance and R_p is the resistance corresponding to the parallel configuration of magnetizations. The resistance drops in Fig. 3 (A and B) result in negative MRs.

Further, we conduct MR measurements under different bias voltages. As shown in Fig. 3C, for 1L device, we observe a decrease of |MR| at higher bias voltages with a maximum appears around zero bias (see details in fig. S6). Such a behavior is possibly due to excitation of magnons, band bending, and involvement of interface states at high voltages (*34*). We observe bias-controlled sign inversion of MR in 2L devices. As shown in Fig. 3D, MR is ~−12.3% at bias voltage of −0.5 mV, while MR is ~12.1% at 0.5 mV (see details in fig. S7). Similar trend has been reported in spin valves with hexagonal boron nitride (*h*-BN) as tunnel barriers (*35*), while detailed mechanism behind the sign inversion in MR around zero bias still needs further studies. We also investigate MR as a function of temperature. As shown in fig. S8, |MR| of 1L device exhibits a $T^{3/2}$ temperature dependence, which can be well understood by the spin wave excitation model (*36*).

It is clear that |MR| of 2L device (in Fig. 3, B and D) is one order of magnitude larger than that of 1L device (in Fig. 3, A and C). To confirm the observed phenomenon, more devices have been studied. Figure 3E shows the maximum measurable |MR| of different devices as a function of R_p, from which an increasing trend of |MR| with R_p is observed. As summarized in Fig. 3F, the averaged |MR| (all measured at the same bias voltage of 1 mV) of 2L devices is notably larger than those of 1L devices and W/O devices. Such results indicate that the FM electrode/molecule interface plays an important role in spin polarization and is very sensitive to the structures of the molecular crystals. Unfortunately, we are not able to further study magneto-transport behaviors of devices with more organic layers, due to the lowered signal-to-noise ratio when the device resistances are increased for 3L devices. MR curves of additional 1L and 2L devices can be found in figs. S9 and S10, respectively. Figures S11 and S12 show MR curves obtained from W/O devices. In addition, we also fabricate a W/O device using the traditional electron-beam lithography and metal evaporation technique and measure its MR for comparison, providing the evidence that nondestructive vdW metal-transfer is beneficial for spin injection (see fig. S13).

Spin polarization at FM electrode/organic molecule interfaces

We present a theoretical model to give a quantitative estimation of spin polarization in our devices. Figure 4A shows the cross-sectional schematics of the device investigated in the experiment. Two FM electrodes connect the heterojunction made of C_8-BTBT and FLG. The device can be simplified as a hybrid structure consisting of a vertical spin transport part with the 2D molecular crystal as spacer and a lateral spin transport part with FLG as conducting channel. A modified drift/diffusion model (*37*, *38*) is used to

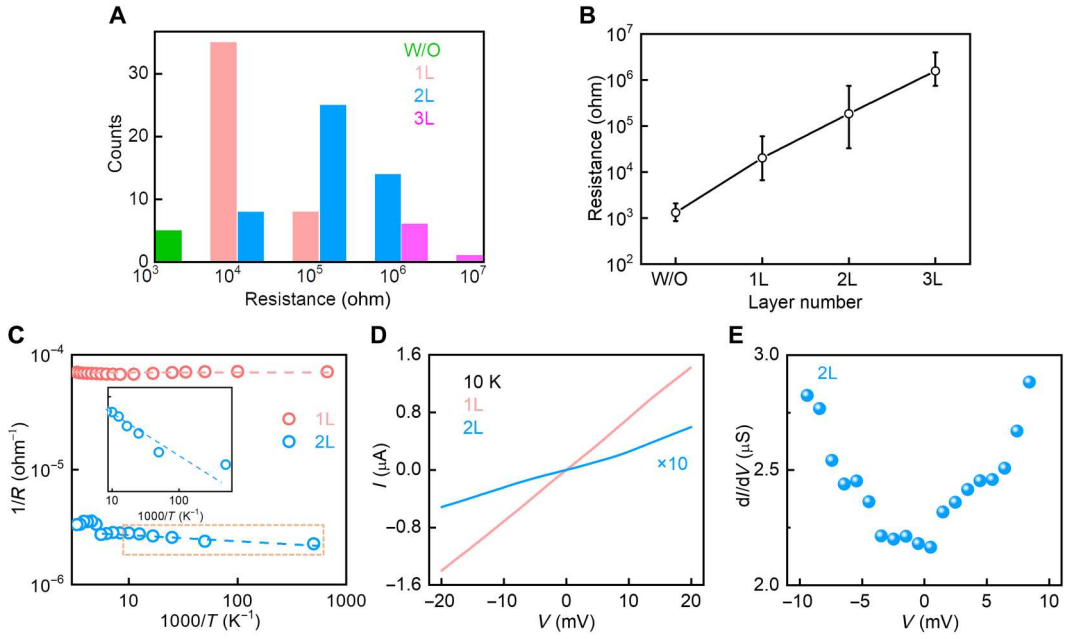

Fig. 2. Electrical characterization of devices in the absence of magnetic field. (**A**) Statistic results of room temperature resistance obtained from more than 100 devices with different layers of organic crystals. (**B**) Averaged resistance as a function of layer number of C_8-BTBT molecules for devices in (A). W/O represents devices without molecular crystals. (**C**) Temperature-dependent conductance of two typical 1L and 2L devices. The inset details the area within the orange dashed box, showing the transport behavior of 2L device at low-temperature regime (2 to 100 K). (**D**) Current-voltage characteristics at low temperature (T = 10 K) of the 1L and 2L devices shown in (C). (**E**) Differential conductance (dI/dV) as a function of bias voltage for the 2L device shown in (D).

characterize the spin transport, giving that

$$\mathrm{MR} = \frac{\Delta R}{R_\mathrm{p}} = \frac{2r_1 r_2}{(2 - r_1^2 - r_2^2)\cosh\left(\frac{L}{l_\mathrm{sf}}\right) + \left[\frac{R_\mathrm{p}}{2R_\mathrm{ch}} + \frac{2R_\mathrm{ch}(1-r_1^2)(1-r_2^2)}{R_\mathrm{p}}\right]\sinh\left(\frac{L}{l_\mathrm{sf}}\right)} \quad (1)$$

where ΔR is the spin-induced resistance change, r_1 and r_2 are the spin polarizations at two terminals of graphene channel (FM1/C_8-BTBT/FLG and FM2/FLG), respectively, L is the channel length, l_sf is the spin diffusion length in FLG, and R_ch is the spin resistance of the channel (R_ch= $\rho l_\mathrm{sf}/W$, where ρ is the resistivity per square of the channel and W is the width of the channel). More details about the model have been elaborated in fig. S14 and note S1.

Using Eq. 1, we can estimate the spin polarization at FM electrode/C_8-BTBT interface, namely, r_1. All the parameters in Eq. 1 are based on the experiment. R_p, L, W, ρ, and r_2 are extracted from the experimental results (see fig. S15 and table S1). Therefore, r_1 only depends on l_sf, which cannot be directly obtained in our experiment. Alternatively, we present spin polarization (r_1) as a function of l_sf, as shown in Fig. 4B. Different curves correspond to different devices (data points in Fig. 3E), respectively. The estimated spin polarization r_1 decreases at longer l_sf. Previous studies have shown that l_sf of FLG can be as long as 70 to 130 μm (*39*). In this range, we can provide an estimation of the spin polarization to be as large as 43.4% for 2L device (Dev. D1). The averaged spin polarization of 2L and 1L devices are 42.2 and 5.1%, respectively, according to our model. Obviously, 2L devices hold much higher spin polarization than 1L devices. It should be pointed out that if l_sf of FLG in our devices is smaller than that reported in the literature, then an even larger spin polarization can be expected. Therefore, the estimated value of spin polarization here should be considered as a lower bound. Moreover, it is worth noting that, in addition to enhancement in spin polarization, our analysis suggests that l_sf of 2L devices are extended for at least one order of magnitude compared with those of W/O devices. This is possibly due to encapsulation of FLG by the synthesized molecular crystal, which is similar to the results reported in BN-encapsulated graphene devices (*40*). Details of analysis can be found in note S1 and figs. S16 and S17.

We further benchmark the performance of our devices with results reported in the literature. Figure 4C marks the spin polarization and |MR| of spin-valve devices that use 2D inorganic and conventional organic semiconductors as nonmagnetic spacers or spin transport channels (see fig. S18 and table S2 for details) (*37*, *41*–*51*). It is clear that a marked enhancement of device performance, not only the measured |MR| but also the estimated spin polarization, can be achieved by precisely controlling the thickness of molecular crystals to increase from 1L to 2L. Our data points of 2L devices locate approaching the upper right corner of the plot, reaching the best level among the previously reported spin valves based on 2D inorganic and conventional organic semiconductors that use similar FM electrodes. Although the spin polarization that we estimated is a lower bound, it is still close to the maximum polarization of the magnetic metal (dashed line in Fig. 4C) (*52*). It is worth noting that we only compare the results of spin valves using cobalt and permalloy as FM electrodes. Using FM materials with higher spin polarization as electrodes (*10*, *53*), even higher MR and interface spin polarization can be achieved. Besides, introducing nonmagnetic insulating layers (*54*) or spin-filter tunnel barriers

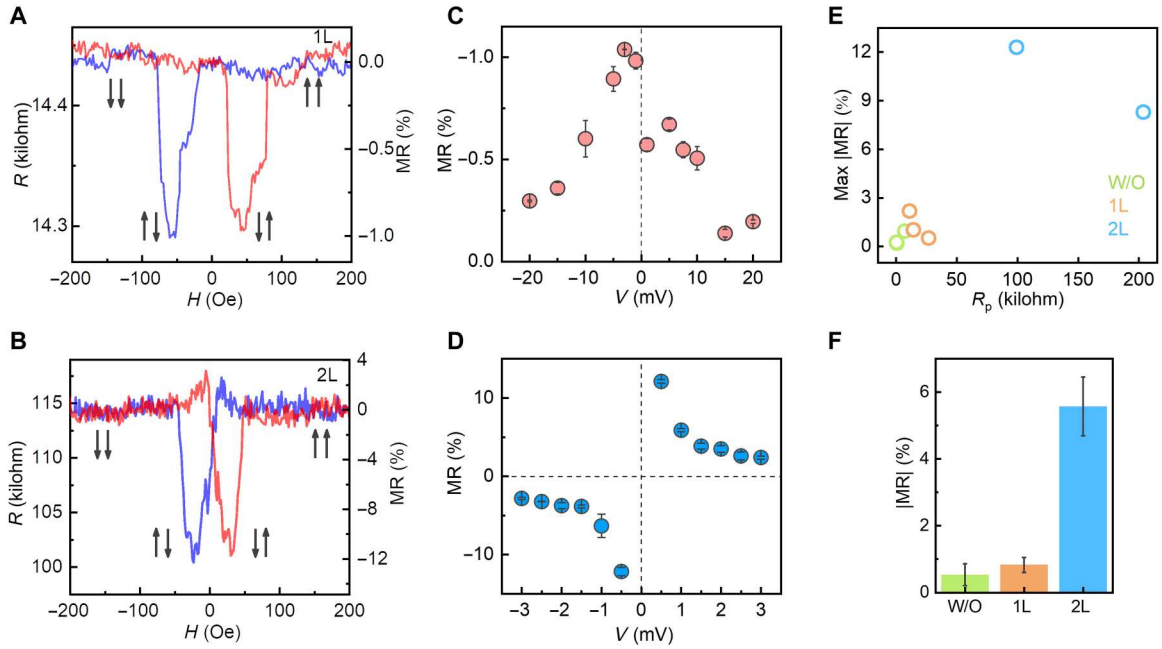

Fig. 3. Magnetoresistance measurements. (**A**) MR of a typical 1L device (Dev. M1) with −1 mV bias voltage. (**B**) MR of a typical 2L device (Dev. D1) with −0.5 mV bias voltage. The blue (red) curves in (A) and (B) correspond to the data obtained through decreasing (increasing) magnetic field. The arrows indicate the magnetization configurations of the two FM electrodes. (**C** and **D**) Bias dependence of MR of (C) 1L device (Dev. M1) and (D) 2L device (Dev. D1). The bias voltage is defined to be positive, when the voltage applied to FM1 is higher than that of FM2. (**E**) Max measurable |MR| as a function of R_p, which is the resistance measured when the magnetization configuration of the two FM electrodes is parallel. Data points are marked with different colors, corresponding to devices with different layers of molecular crystals. (**F**) Bar diagram illustrating the averaged |MR| measured at the same bias voltage of 1 mV for devices in (E). All measurements for obtaining (A) to (F) are conducted at a temperature of 10 K. The data in (E) and (F) are listed in table S1.

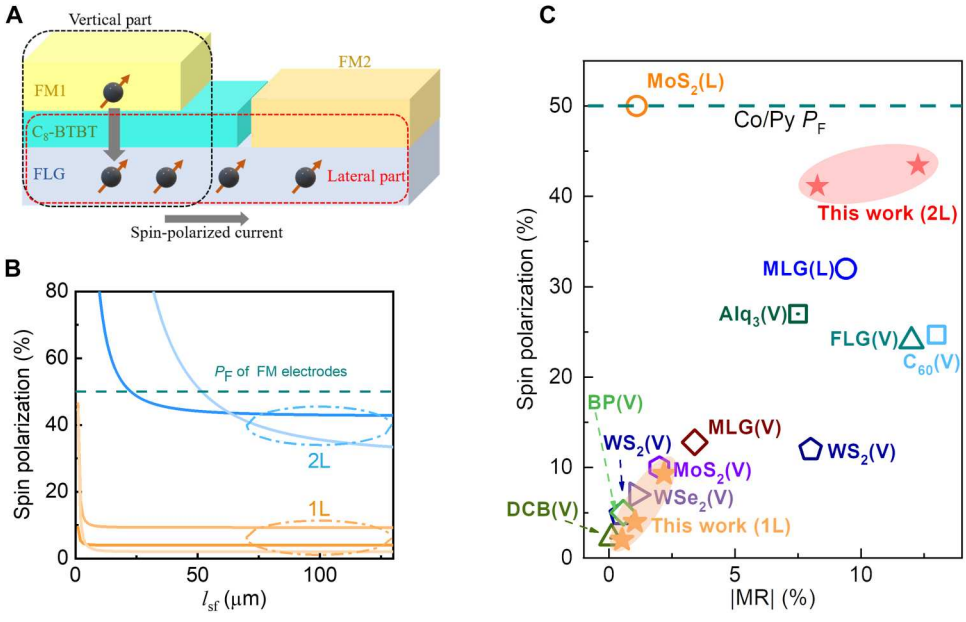

Fig. 4. Estimating interface spin polarization and benchmarking device performance. (**A**) Schematics of spin transport in the device. (**B**) Calculated spin polarization at different l_{sf}. Each curve corresponds to one device (one data point in Fig. 3E). (**C**) Benchmarking of |MR| and spin polarization with results reported in the literature. The dashed lines in (B) and (C) indicate the maximum spin polarization values (P_F) of the FM metals. We compare our results with those obtained from devices based on 2D inorganic and conventional organic semiconductors. "L" and "V" mark data from lateral and vertical spin valves, respectively. Only devices using cobalt and permalloy as FM electrodes are summarized here. Details of data points are presented in fig. S18 and table S2.

(*41*, *55*, *56*) can further improve the spin injection efficiency. We believe that with these optimizations, devices with larger MR (*10*, *55*) and higher working temperature (*57*) can be expected based on our demonstration of high-quality FM electrode/molecule interfaces.

DFT calculations of spin-dependent DOS

The distinct difference in spin polarization between 1L and 2L devices is unlikely from extrinsic factors, such as traps or impurities, since it is evidenced by multiple devices. Meanwhile, although there are several interfaces in our OSV devices, the main contribution to the difference should come from the FM1/C_8-BTBT interface, since other interfaces are built using the same fabrication process, thus are supposed to be similar. Therefore, to understand the role of FM1/C_8-BTBT interface, we carry out DFT calculations for 1L and 2L C_8-BTBT crystals, respectively.

The well-defined FM1/C_8-BTBT interfaces allow us to perform DFT calculations on spin-dependent DOS (see Materials and Methods for details). The structures of 1L and 2L C_8-BTBT used in our calculations are determined in previous studies (*22*, *28*), as illustrated in Fig. 1 (A and B). We neglect IL in the calculation to lower the size of the model. Figure 5 (A and D) shows the spin density distributions at Fe-Ni/MLG/C_8-BTBT interfaces. For the case of the 1L structure (see Fig. 5A), spin density almost distributes on Fe-Ni and MLG layers, indicating that spin-dependent interfacial coupling with the organic layer is weak. However, modifying the packing configuration of organic layer, polarized spin density in organic layer is generated obviously (see Fig. 5D). Then, for the case of the 2L structure, the top spin-polarized organic layer can effectively transport spins to bottom organic layer because of the small conductance difference between these two organic layers, which would minimize the spin flip scattering and prevent the spin-backflow processes simultaneously. Thus, a stronger spin injection is achieved, leading to a larger MR. Moreover, the spin dependence of interfacial DOS further confirms the key role of molecular packing. Spin-dependent DOSs of the 2L structure are much larger than those of the 1L structure (see Fig. 5, B and E). Meanwhile, the net spin DOS calculations also demonstrate the distinct difference. As shown in Fig. 5 (C and F), the net spin DOS of the 2L structure is pronounced while that of the 1L structure has almost vanished. Such notable difference in calculated spin density distribution is in qualitative agreement with the different spin polarizations estimated for 1L and 2L devices. Physically, spin carriers are more effectively polarized at the interface between the FM electrode and 2L C_8-BTBT, compared with 1L C_8-BTBT. Therefore, it results in a more pronounced spin-valve effect and larger |MR| to be measured, assuming that other interfaces remain the same.

DISCUSSION

As shown in Fig. 5, spin polarization is strongly modulated by molecular packing motifs. Two possible aspects are involved: (i) One additional layer is included in 2L crystals, compared with 1L crystals; (ii) in 2L crystals, molecules in the layer adjacent to the FM electrode stand vertically, while they tilt in 1L crystals. Therefore, we calculate the spin-dependent DOSs of two hypothetical structures, that is, monolayer crystal in which molecules stand vertically (referred to as "vertical monolayer"; see fig. S19A) and bilayer crystal in which molecules of both layers tilt for the same angle (referred to as "tilted bilayer"; see fig. S19D). Unexpectedly, compared with the 2L structure shown in Fig. 5D, much less polarized spin density distributions are found for both the vertical monolayer and tilted bilayer structures (see fig. S19, A and D). Accordingly, the calculated spin-dependent and net spin DOSs based on vertical monolayer (fig. S19, B and C) and tilted bilayer (fig. S19, E and F) are also smaller than those of the 2L structure, exhibiting the same trend. These results suggest that the spin polarization is very sensitive to the packing structure, while it is difficult to attribute the dominant role to either the additional layer or the tilted molecules' orientation. It appears that both aspects interplay to result in an enhanced polarized spin density distributed in the 2L structure. In addition, we further calculate spin-dependent DOS distributions of Co/MLG/C_8-BTBT interfaces, as shown in fig. S20. It also

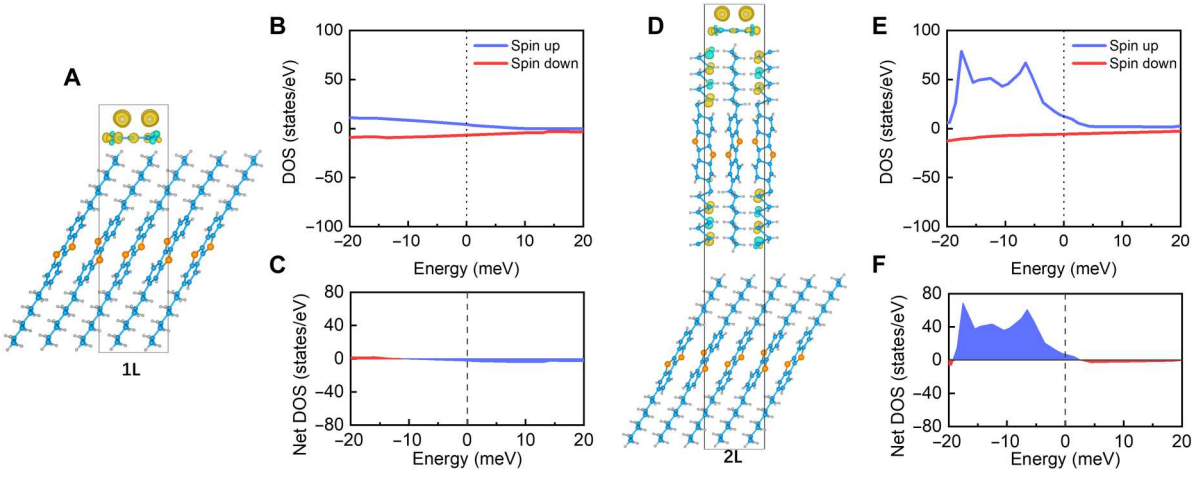

Fig. 5. DFT calculations of spin-dependent DOS. Schematic illustration of Fe-Ni/MLG/C_8-BTBT stacks of (**A**) 1L and (**D**) 2L structures for DFT calculations, respectively. Calculated spin-dependent DOS and net spin DOS for (**B** and **C**) 1L and (**E** and **F**) 2L structures, respectively. The black boxes in (A) and (D) mark the unit cell used in DFT calculations, which are overlaid by the spin-dependent charge density distributions (yellow and cyan represent spin up and spin down, respectively). The net DOSs in (C) and (F) are directly calculated from (B) and (E), respectively.

demonstrates enhanced polarized spin density distributed in the 2L structure, further confirming the key role of molecular packing on interface spin polarization. We would like to point out that besides the packing structure, additional reasons, such as interlayer coupling, may also contribute to the distinct spin polarization difference, which invites further studies to fully understand the FM electrode/molecule interfaces.

Our devices are based on vdW organic/inorganic heterostructures, providing the possibilities to make use of the combined advantages of different material classes at 2D limit (*58*). Moreover, with the boosting diversity of 2D molecular crystals, our devices can be extended to other 2D organic crystals (*59*, *60*), allowing the realization of multifunctional spintronic devices. Meanwhile, unlike previously reported vertical OSVs, the device architecture demonstrated here is compatible with gating technology, laying the foundation of gate-controlled organic spintronic devices. On the basis of the demonstrated high-quality FM electrode/molecule interface and large interface spin polarization, high-performance lateral OSVs are expected to unlock the great potential that organic materials host for spintronic applications.

In conclusion, we demonstrate that it is possible to build OSVs with high-quality FM electrode/molecule interfaces by combining highly ordered ultrathin single-crystalline organic crystals and nondestructive vdW magnetic-electrode integration technology. Our devices not only demonstrate excellent device performance but also provide a powerful platform to explore the relationship between interface spin polarization and molecular packing at 2D limit, which is technically challenging for conventional OSVs. Our experimental results and theoretical analysis reveal that the molecular packing structure plays a key role in engineering spin polarization at FM metal/molecule interfaces. Given the feasibility of synthesizing large-area 2D molecular crystals and processing graphene-assisted vdW magnetic-electrode integration, high-performance organic spintronic devices with controllable FM metal/molecule interfaces are within reach.

MATERIALS AND METHODS

Device fabrication and characterization

First, we exfoliated FLG flakes on the Si wafer with 285-nm SiO_2. Second, the prefabricated cobalt multilayer FM electrode (FM2 in Fig. 1E) was mechanically released and transferred at one side of a chosen exfoliated FLG flake using a micrometer-size probe. Then, we grew the 2D molecular crystal via vdW epitaxy. Last, the permalloy multilayer FM electrode (FM1 in Fig. 1E) was transferred to the molecular crystal as the other FM electrode. During transferring electrodes, the bottom surfaces of the multilayer FM electrodes were not exposed to any solvents. The corresponding fabrication process is illustrated in fig. S2.

We used cross-sectional TEM to characterize the FM electrode/molecule interface. The TEM specimens were prepared using a FEI Helios 600i dual-beam focused ion beam system. After that, the specimens were characterized using a high-resolution FEI Talos F200X with an acceleration voltage of 200 kV equipped with an energy-dispersive spectroscopy detector.

Multilayer electrode fabrication

First, large-area MLG films grown on copper foils by CVD were transferred onto 285-nm SiO_2/Si substrates using polymethyl methacrylate as supporting layers. Then, the substrates were soaked overnight in the acetone, followed with 30 min of annealing at 350°C under H_2 and Ar atmosphere to remove residual polymers from MLG's surface. FM metal (cobalt or permalloy, 10 nm) and Au (90 nm) were then deposited sequentially on MLG by electron-beam evaporation under high vacuum of 5×10^{-8} torr. A metal shadow mask was settled upon MLG to shape electrodes to sizes of 200 μm by 20 μm.

2D molecular crystal growth and characterization

To synthesize high-quality 2D molecular crystals, we exploited the epitaxy of molecular crystals on exfoliated FLG flakes. A home-built tube furnace was adopted to grow 2D molecular crystals. The C_8-BTBT powder was placed at the center of the heating zone. A substrate with a mechanically exfoliated FLG covered by one FM electrode at one end (FM2 in Fig. 1E) was located downstream. The growth temperature was set around 110°C, with a pressure of 1×10^{-4} torr. High-resolution and regular AFM measurements were used to characterize the surface morphology and thickness information of the C_8-BTBT crystals.

Transport measurements

Magneto-transport measurements were performed using a physical properties measurement system with temperature from 1.5 to 300 K and a maximum magnetic field of 14 T. The in-plane magnetic field was applied parallel to the FM electrodes. Keithley 2450 was used to apply bias voltage V and to measure device current I. To avoid possible damages to ultrathin molecular crystals during the cooling process, the cooling rate was controlled at 0.1 K/min.

Details of DFT calculations

All calculations were performed using the Quantum ESPRESSO program on the basis of DFT. A unit cell consists of two couples of Fe-Ni atoms and two (four) molecules for the 1L (2L) structure. Hexagonal carbon rings were inserted between Fe-Ni atoms and C_8-BTBT in simulations to take the influence of the partially damaged MLG layer into consideration. In all calculations, vdW interactions were considered at FM metal/MLG/molecule interfaces and interlayer of molecules. A vacuum space of 40 Å was applied along the z direction. The projected augmented wave method was used to describe the electron-ion interactions. The exchange-correlation interaction was treated by the generalized gradient approximation in the form of Perdew-Burke-Ernzerhof functional. The cutoff energy of the plane wave was set to 500 eV. A k-grid of $7 \times 5 \times 1$ was used in electronic structure calculations. The convergence criteria for energy and force were set to 1×10^{-5} eV and 0.01 eV/Å, respectively.

Supplementary Materials

This PDF file includes:

Note S1
Figs. S1 to S20
Tables S1 and S2
References

REFERENCES AND NOTES

1. Z. H. Xiong, D. Wu, Z. Valy Vardeny, J. Shi, Giant magnetoresistance in organic spin-valves. *Nature* **427**, 821–824 (2004).

2. S. Sanvito, Molecular spintronics. *Chem. Soc. Rev.* **40**, 3336–3355 (2011).
3. M. Cinchetti, V. A. Dediu, L. E. Hueso, Activating the molecular spinterface. *Nat. Mater.* **16**, 507–515 (2017).
4. S. Ding, Y. Tian, H. Wang, Z. Zhou, W. Mi, Z. Ni, Y. Zou, H. Dong, H. Gao, D. Zhu, W. Hu, Reliable spin valves of conjugated polymer based on mechanically transferrable top electrodes. *ACS Nano* **12**, 12657–12664 (2018).
5. S.-J. Wang, D. Venkateshvaran, M. R. Mahani, U. Chopra, E. R. McNellis, R. Di Pietro, S. Schott, A. Wittmann, G. Schweicher, M. Cubukcu, K. Kang, R. Carey, T. J. Wagner, J. N. M. Siebrecht, D. P. G. H. Wong, I. E. Jacobs, R. O. Aboljadayel, A. Ionescu, S. A. Egorov, S. Mueller, O. Zadvorna, P. Skalski, C. Jellett, M. Little, A. Marks, I. McCulloch, J. Wunderlich, J. Sinova, H. Sirringhaus, Long spin diffusion lengths in doped conjugated polymers due to enhanced exchange coupling. *Nat. Electron.* **2**, 98–107 (2019).
6. D. Li, G. Yu, Innovation of materials, devices, and functionalized interfaces in organic spintronics. *Adv. Funct. Mater.* **31**, 2100550 (2021).
7. W. Yang, Q. Shi, T. Miao, Q. Li, P. Cai, H. Liu, H. Lin, Y. Bai, Y. Zhu, Y. Yu, L. Deng, W. Wang, L. Yin, D. Sun, X. G. Zhang, J. Shen, Achieving large and nonvolatile tunable magnetoresistance in organic spin valves using electronic phase separated manganites. *Nat. Commun.* **10**, 3877 (2019).
8. K. V. Raman, A. M. Kamerbeek, A. Mukherjee, N. Atodiresei, T. K. Sen, P. Lazić, V. Caciuc, R. Michel, D. Stalke, S. K. Mandal, S. Blügel, M. Münzenberg, J. S. Moodera, Interface-engineered templates for molecular spin memory devices. *Nature* **493**, 509–513 (2013).
9. Y.-H. Kim, Y. Zhai, H. Lu, X. Pan, C. Xiao, E. A. Gaulding, S. P. Harvey, J. J. Berry, Z. V. Vardeny, J. M. Luther, M. C. Beard, Chiral-induced spin selectivity enables a room-temperature spin light-emitting diode. *Science* **371**, 1129–1133 (2021).
10. C. Barraud, P. Seneor, R. Mattana, S. Fusil, K. Bouzehouane, C. Deranlot, P. Graziosi, L. Hueso, I. Bergenti, V. Dediu, F. Petroff, A. Fert, Unravelling the role of the interface for spin injection into organic semiconductors. *Nat. Phys.* **6**, 615–620 (2010).
11. A. Wittmann, G. Schweicher, K. Broch, J. Novak, V. Lami, D. Cornil, E. R. McNellis, O. Zadvorna, D. Venkateshvaran, K. Takimiya, Y. H. Geerts, J. Cornil, Y. Vaynzof, J. Sinova, S. Watanabe, H. Sirringhaus, Tuning spin current injection at ferromagnet-nonmagnet interfaces by molecular design. *Phys. Rev. Lett.* **124**, 027204 (2020).
12. A. Bedoya-Pinto, S. G. Miralles, S. Vélez, A. Atxabal, P. Gargiani, M. Valvidares, F. Casanova, E. Coronado, L. E. Hueso, Interface-assisted sign inversion of magnetoresistance in spin valves based on novel lanthanide quinoline molecules. *Adv. Funct. Mater.* **28**, 1702099 (2018).
13. H. Isshiki, K. Kondou, S. Takizawa, K. Shimose, T. Kawabe, E. Minamitani, N. Yamaguchi, F. Ishii, A. Shiotari, Y. Sugimoto, S. Miwa, Y. Otani, Realization of spin-dependent functionality by covering a metal surface with a single layer of molecules. *Nano Lett.* **19**, 7119–7123 (2019).
14. P. Martin, B. Dlubak, R. Mattana, P. Seneor, M.-B. Martin, T. Henner, F. Godel, A. Sander, S. Collin, L. Chen, S. Suffit, F. Mallet, P. Lafarge, M. L. Della Rocca, A. Droghetti, C. Barraud, Combined spin filtering actions in hybrid magnetic junctions based on organic chains covalently attached to graphene. *Nanoscale* **14**, 12692–12702 (2022).
15. J. Devkota, R. Geng, R. C. Subedi, T. D. Nguyen, Organic spin valves: A review. *Adv. Funct. Mater.* **26**, 3881–3898 (2016).
16. H. Nakayama, T. Yamamoto, H. An, K. Tsuda, Y. Einaga, K. Ando, Molecular engineering of Rashba spin-charge converter. *Sci. Adv.* **4**, eaar3899 (2018).
17. Y. Zhong, B. Cheng, C. Park, A. Ray, S. Brown, F. Mujid, J.-U. Lee, H. Zhou, J. Suh, K.-H. Lee, A. J. Mannix, K. Kang, S. J. Sibener, D. A. Muller, J. Park, Wafer-scale synthesis of monolayer two-dimensional porphyrin polymers for hybrid superlattices. *Science* **366**, 1379–1384 (2019).
18. Y. Shi, L. Jiang, J. Liu, Z. Tu, Y. Hu, Q. Wu, Y. Yi, E. Gann, C. R. McNeill, H. Li, W. Hu, D. Zhu, H. Sirringhaus, Bottom-up growth of n-type monolayer molecular crystals on polymeric substrate for optoelectronic device applications. *Nat. Commun.* **9**, 2933 (2018).
19. A. Yamamura, S. Watanabe, M. Uno, M. Mitani, C. Mitsui, J. Tsurumi, N. Isahaya, Y. Kanaoka, T. Okamoto, J. Takeya, Wafer-scale, layer-controlled organic single crystals for high-speed circuit operation. *Sci. Adv.* **4**, eaao5758 (2018).
20. N. Kasuya, J. Tsurumi, T. Okamoto, S. Watanabe, J. Takeya, Two-dimensional hole gas in organic semiconductors. *Nat. Mater.* **20**, 1401–1406 (2021).
21. Z. Luo, B. Peng, J. Zeng, Z. Yu, Y. Zhao, J. Xie, R. Lan, Z. Ma, L. Pan, K. Cao, Y. Lu, D. He, H. Ning, W. Meng, Y. Yang, X. Chen, W. Li, J. Wang, D. Pan, X. Tu, W. Huo, X. Huang, D. Shi, L. Li, M. Liu, Y. Shi, X. Feng, P. K. L. Chan, X. Wang, Sub-thermionic, ultra-high-gain organic transistors and circuits. *Nat. Commun.* **12**, 1928 (2021).
22. D. He, Y. Zhang, Q. Wu, R. Xu, H. Nan, J. Liu, J. Yao, Z. Wang, S. Yuan, Y. Li, Y. Shi, J. Wang, Z. Ni, L. He, F. Miao, F. Song, H. Xu, K. Watanabe, T. Taniguchi, J.-B. Xu, X. Wang, Two-dimensional quasi-freestanding molecular crystals for high-performance organic field-effect transistors. *Nat. Commun.* **5**, 5162 (2014).
23. C.-H. Lee, T. Schiros, E. J. G. Santos, B. Kim, K. G. Yager, S. J. Kang, S. Lee, J. Yu, K. Watanabe, T. Taniguchi, J. Hone, E. Kaxiras, C. Nuckolls, P. Kim, Epitaxial growth of molecular crystals on van der Waals substrates for high-performance organic electronics. *Adv. Mater.* **26**, 2812–2817 (2014).
24. Q. Tang, Y. Tong, H. Li, Z. Ji, L. Li, W. Hu, Y. Liu, D. Zhu, High-performance air-stable bipolar field-effect transistors of organic single-crystalline ribbons with an air-gap dielectric. *Adv. Mater.* **20**, 1511–1515 (2008).
25. Y. Liu, J. Guo, E. Zhu, L. Liao, S.-J. Lee, M. Ding, I. Shakir, V. Gambin, Y. Huang, X. Duan, Approaching the Schottky–Mott limit in van der Waals metal–semiconductor junctions. *Nature* **557**, 696–700 (2018).
26. G. Liu, Z. Tian, Z. Yang, Z. Xue, M. Zhang, X. Hu, Y. Wang, Y. Yang, P. K. Chu, Y. Mei, L. Liao, W. Hu, Z. Di, Graphene-assisted metal transfer printing for wafer-scale integration of metal electrodes and two-dimensional materials. *Nat. Electron.* **5**, 275–280 (2022).
27. L. Wang, P. Wang, J. Huang, B. Peng, C. Jia, Q. Qian, J. Zhou, D. Xu, Y. Huang, X. Duan, A general one-step plug-and-probe approach to top-gated transistors for rapidly probing delicate electronic materials. *Nat. Nanotechnol.* **17**, 1206–1213 (2022).
28. D. He, J. Qiao, L. Zhang, J. Wang, T. Lan, J. Qian, Y. Li, Y. Shi, Y. Chai, W. Lan, L. K. Ono, Y. Qi, J.-B. Xu, W. Ji, X. Wang, Ultrahigh mobility and efficient charge injection in monolayer organic thin-film transistors on boron nitride. *Sci. Adv.* **3**, e1701186 (2017).
29. W. Han, R. K. Kawakami, M. Gmitra, J. Fabian, Graphene spintronics. *Nat. Nanotechnol.* **9**, 794–807 (2014).
30. A. Avsar, H. Ochoa, F. Guinea, B. Özyilmaz, B. J. van Wees, I. J. Vera-Marun, Colloquium: Spintronics in graphene and other two-dimensional materials. *Rev. Mod. Phys.* **92**, 021003 (2020).
31. B. Peng, K. Cao, A. H. Y. Lau, M. Chen, Y. Lu, P. K. L. Chan, Crystallized monolayer semiconductor for ohmic contact resistance, high intrinsic gain, and high current density. *Adv. Mater.* **32**, 2002281 (2020).
32. J. G. Simmons, Generalized formula for the electric tunnel effect between similar electrodes separated by a thin insulating film. *J. Appl. Phys.* **34**, 1793–1803 (1963).
33. J. Appelbaum, "*s–d*" exchange model of zero-bias tunneling anomalies. *Phys. Rev. Lett.* **17**, 91–95 (1966).
34. J. S. Moodera, J. Nowak, R. J. M. van de Veerdonk, Interface magnetism and spin wave scattering in ferromagnet-insulator-ferromagnet tunnel junctions. *Phys. Rev. Lett.* **80**, 2941–2944 (1998).
35. M. Piquemal-Banci, R. Galceran, F. Godel, S. Caneva, M.-B. Martin, R. S. Weatherup, P. R. Kidambi, K. Bouzehouane, S. Xavier, A. Anane, F. Petroff, A. Fert, S. M.-M. Dubois, J.-C. Charlier, J. Robertson, S. Hofmann, B. Dlubak, P. Seneor, Insulator-to-metallic spin-filtering in 2D-magnetic tunnel junctions based on hexagonal boron nitride. *ACS Nano* **12**, 4712–4718 (2018).
36. C. H. Shang, J. Nowak, R. Jansen, J. S. Moodera, Temperature dependence of magnetoresistance and surface magnetization in ferromagnetic tunnel junctions. *Phys. Rev. B* **58**, R2917–R2920 (1998).
37. B. Dlubak, M.-B. Martin, C. Deranlot, B. Servet, S. Xavier, R. Mattana, M. Sprinkle, C. Berger, W. A. De Heer, F. Petroff, A. Anane, P. Seneor, A. Fert, Highly efficient spin transport in epitaxial graphene on SiC. *Nat. Phys.* **8**, 557–561 (2012).
38. H. Jaffrès, J. M. George, A. Fert, Spin transport in multiterminal devices: Large spin signals in devices with confined geometry. *Phys. Rev. B* **82**, 140408 (2010).
39. W. Yan, L. C. Phillips, M. Barbone, S. J. Hämäläinen, A. Lombardo, M. Ghidini, X. Moya, F. Maccherozzi, S. van Dijken, S. S. Dhesi, A. C. Ferrari, N. D. Mathur, Long spin diffusion length in few-layer graphene flakes. *Phys. Rev. Lett.* **117**, 147201 (2016).
40. M. H. D. Guimarães, P. J. Zomer, J. Ingla-Aynés, J. C. Brant, N. Tombros, B. J. van Wees, Controlling spin relaxation in hexagonal BN-encapsulated graphene with a transverse electric field. *Phys. Rev. Lett.* **113**, 086602 (2014).
41. E. D. Cobas, O. M. J. van't Erve, S.-F. Cheng, J. C. Culbertson, G. G. Jernigan, K. Bussman, B. T. Jonker, Room-temperature spin filtering in metallic ferromagnet–multilayer graphene–ferromagnet junctions. *ACS Nano* **10**, 10357–10365 (2016).
42. W. Li, L. Xue, H. D. Abruña, D. C. Ralph, Magnetic tunnel junctions with single-layer-graphene tunnel barriers. *Phys. Rev. B* **89**, 184418 (2014).
43. A. Dankert, P. Pashaei, M. V. Kamalakar, A. P. S. Gaur, S. Sahoo, I. Rungger, A. Narayan, K. Dolui, M. A. Hoque, R. S. Patel, M. P. de Jong, R. S. Katiyar, S. Sanvito, S. P. Dash, Spin-polarized tunneling through chemical vapor deposited multilayer molybdenum disulfide. *ACS Nano* **11**, 6389–6395 (2017).
44. K. Zhao, Y. Xing, J. Han, J. Feng, W. Shi, B. Zhang, Z. Zeng, Magnetic transport property of NiFe/WSe_2/NiFe spin valve structure. *J. Magn. Magn. Mater.* **432**, 10–13 (2017).
45. L. Xu, J. Feng, K. Zhao, W. Lv, X. Han, Z. Liu, X. Xu, H. Huang, Z. Zeng, Magnetoresistance effect in NiFe/BP/NiFe vertical spin valve devices. *Adv. Condens. Matter Phys.* **2017**, 9042823 (2017).
46. M. Z. Iqbal, M. W. Iqbal, S. Siddique, M. F. Khan, S. M. Ramay, Room temperature spin valve effect in NiFe/WS_2/Co junctions. *Sci. Rep.* **6**, 21038 (2016).
47. V. Zatko, M. Galbiati, S. M.-M. Dubois, M. Och, P. Palczynski, C. Mattevi, P. Brus, O. Bezencenet, M.-B. Martin, B. Servet, J.-C. Charlier, F. Godel, A. Vecchiola, K. Bouzehouane,

S. Collin, F. Petroff, B. Dlubak, P. Seneor, Band-structure spin-filtering in vertical spin valves based on chemical vapor deposited WS_2. *ACS Nano* **13**, 14468–14476 (2019).
48. S. Liang, H. Yang, P. Renucci, B. Tao, P. Laczkowski, S. Mc-Murtry, G. Wang, X. Marie, J.-M. George, S. Petit-Watelot, A. Djeffal, S. Mangin, H. Jaffrès, Y. Lu, Electrical spin injection and detection in molybdenum disulfide multilayer channel. *Nat. Commun.* **8**, 14947 (2017).
49. M. Gobbi, F. Golmar, R. Llopis, F. Casanova, L. E. Hueso, Room-temperature spin transport in C_{60}-based spin valves. *Adv. Mater.* **23**, 1609–1613 (2011).
50. T. S. Santos, J. S. Lee, P. Migdal, I. C. Lekshmi, B. Satpati, J. S. Moodera, Room-temperature tunnel magnetoresistance and spin-polarized tunneling through an organic semiconductor barrier. *Phys. Rev. Lett.* **98**, 016601 (2007).
51. N. Zheng, X. Wang, Y. Zheng, D. Li, Z. Lin, W. Zhang, K.-j. Jin, G. Yu, Negative magnetoresistance behavior in polymer spin valves based on donor-acceptor conjugated molecules. *Adv. Mater. Interfaces* **7**, 2000868 (2020).
52. J. S. Moodera, G. Mathon, Spin polarized tunneling in ferromagnetic junctions. *J. Magn. Magn. Mater.* **200**, 248–273 (1999).
53. Y. Zheng, Y. Feng, D. Gao, N. Zheng, D. Li, L. Jiang, X. Wang, K. Jin, G. Yu, Magnetoresistance and spinterface of organic spin valves based on diketopyrrolopyrrole polymers. *Adv. Electron. Mater.* **5**, 1900318 (2019).
54. W. Han, K. Pi, K. M. McCreary, Y. Li, J. J. I. Wong, A. G. Swartz, R. K. Kawakami, Tunneling spin injection into single layer graphene. *Phys. Rev. Lett.* **105**, 167202 (2010).
55. V. Zatko, S. M. M. Dubois, F. Godel, M. Galbiati, J. Peiro, A. Sander, C. Carretero, A. Vecchiola, S. Collin, K. Bouzehouane, B. Servet, F. Petroff, J.-C. Charlier, M.-B. Martin, B. Dlubak, P. Seneor, Almost perfect spin filtering in graphene-based magnetic tunnel junctions. *ACS Nano* **16**, 14007–14016 (2022).
56. M. Piquemal-Banci, R. Galceran, S. M. M. Dubois, V. Zatko, M. Galbiati, F. Godel, M.-B. Martin, R. S. Weatherup, F. Petroff, A. Fert, J.-C. Charlier, J. Robertson, S. Hofmann, B. Dlubak, P. Seneor, Spin filtering by proximity effects at hybridized interfaces in spin-valves with 2D graphene barriers. *Nat. Commun.* **11**, 5670 (2020).
57. X. Sun, M. Gobbi, A. Bedoya-Pinto, O. Txoperena, F. Golmar, R. Llopis, A. Chuvilin, F. Casanova, L. E. Hueso, Room-temperature air-stable spin transport in bathocuproine-based spin valves. *Nat. Commun.* **4**, 2794 (2013).
58. X. Xu, Z. Lou, S. Cheng, P. C. Y. Chow, N. Koch, H.-M. Cheng, Van der Waals organic/inorganic heterostructures in the two-dimensional limit. *Chem* **7**, 2989–3026 (2021).
59. J. Liu, H. Zhang, H. Dong, L. Meng, L. Jiang, L. Jiang, Y. Wang, J. Yu, Y. Sun, W. Hu, A. J. Heeger, High mobility emissive organic semiconductor. *Nat. Commun.* **6**, 10032 (2015).
60. H. Zhao, Y. Zhao, Y. Song, M. Zhou, W. Lv, L. Tao, Y. Feng, B. Song, Y. Ma, J. Zhang, J. Xiao, Y. Wang, D.-H. Lien, M. Amani, H. Kim, X. Chen, Z. Wu, Z. Ni, P. Wang, Y. Shi, H. Ma, X. Zhang, J.-B. Xu, A. Troisi, A. Javey, X. Wang, Strong optical response and light emission from a monolayer molecular crystal. *Nat. Commun.* **10**, 5589 (2019).
61. W. Han, K. Pi, W. Bao, K. M. McCreary, Y. Li, W. H. Wang, C. N. Lau, R. K. Kawakami, Electrical detection of spin precession in single layer graphene spin valves with transparent contacts. *Appl. Phys. Lett.* **94**, 222109 (2009).
62. E. Cobas, A. L. Friedman, O. M. J. van't Erve, J. T. Robinson, B. T. Jonker, Graphene as a tunnel barrier: Graphene-based magnetic tunnel junctions. *Nano Lett.* **12**, 3000–3004 (2012).
63. V. M. Karpan, G. Giovannetti, P. A. Khomyakov, M. Talanana, A. A. Starikov, M. Zwierzycki, J. van den Brink, G. Brocks, P. J. Kelly, Graphite and graphene as perfect spin filters. *Phys. Rev. Lett.* **99**, 176602 (2007).

Acknowledgments: We would like to thank X. Wang (Nanjing University) and W. Han (Peking University) for the support in this work. We also thank W. Xing (Peking University) and X. Xu (Tsinghua Shenzhen International Graduate School) for fruitful discussions. **Funding:** The authors acknowledge support from the Natural Science Foundation of Jiangsu Province (grant no. BK20220397), the National Natural Science Foundation of China (grant nos. 62204130, 12274397, 61974070, and 62288102), the National Funds for Distinguished Young Scientists (grant no. 61825503), the Natural Science Foundation of the Higher Education Institutions of Jiangsu Province (grant no. 22KJB510010), the Science Foundation of Nanjing University of Posts and Telecommunications (grant no. NY221116), Guangdong Province Research and Development in Key Fields from Guangdong Greater Bay Area Institute of Integrated Circuit and System (no. 2021B0101280002), and Guangzhou City Research and Development Program in Key Field (no. 20210302001). **Author contributions:** Z.L. and Q.Z. conceived the project. Z.L. and X.S. designed the experiment. Z.L., X.S., Y.Y., J.Z., Y.L., D.H., H.Z., L.G., Z.Y., W.N., H.S., Y.X., and S.L. contributed to sample preparation, characterization, device fabrication, measurements, and data analysis. Z.L. and X. Liu prepared the TEM specimens. X. Lu and W.Q. carried out the DFT calculations. Z.L. and X.S. cowrote the manuscript with inputs from other authors. All authors contributed to discussions. **Competing interests:** The authors declare that they have no competing interests. **Data and materials availability:** All data needed to evaluate the conclusions in the paper are present in the paper and/or the Supplementary Materials.

Submitted 19 September 2022
Accepted 3 March 2023
Published 5 April 2023
10.1126/sciadv.ade9126